Energy &
Environmental
Science

# Pursuing Graphite−Based K−Ion O2 Batteries: A Lesson from Li−Ion Batteries

SCHOLARONE™
Manuscripts

## ARTICLE

# Pursuing Graphite−Based K−Ion O$_2$ Batteries: A Lesson from Li−Ion Batteries

Lei Qin,[a] Songwei Zhang,[a] Jingfeng Zheng,[a] Yu Lei,[b] Dengyun Zhai,*[b] and Yiying Wu*[a]

The replacement of lithium metal by lithium intercalated graphite was crucial for developing safe lithium−ion batteries. Superoxide−based potassium−oxygen batteries represent an exciting metal−oxygen battery with the highest energy efficiencies. However, using potassium metal is a more serious safety threat than lithium. Herein, we explore the possibility of graphite-intercalation anode for potassium−ion oxygen batteries (PIOBs) with enhanced safety. This work demonstrates for the first time that establishing an artificial potassium salt-rich solid electrolyte interphase (SEI) enables reversible graphite-intercalation anode (249.6 mAh g$^{-1}$ after 600 cycles) in a potassium bis(trifluoromethanesulfonyl)imide (KTFSI)-based localized high-concentration electrolyte. Such an electrolyte is stable with the superoxide cathode. The PIOB delivers energy efficiencies above 90% at a depth of discharge (DOD) of 25% for 80 cycles. Three-electrode measurement shows that its overpotential mainly comes from the anode. The lifespan is limited to the gradual degradation of artificial SEI caused by oxygen crossover. This work represents a step towards achieving the holistic anode-electrolyte-cathode compatibility in a PIOB and its realistic evaluation under controlled DOD.

## Broader context

The superoxide−based potassium−oxygen batteries (POBs) have promised high energy densities, high energy efficiencies, and low costs, which are promising alternatives to the current state-of-the-art lithium−ion batteries. However, the high reactivity of metallic potassium (K) has severe reactions with electrolyte, which leads to low anode reversibility and critical safety concerns and limits the development of practical POBs. Here, we select the graphite as the anode with the enhanced safety and develop an artificial protective interphase on the graphite surface to enable reversible graphite-intercalation. The potassium bis(trifluoromethanesulfonyl)imide (KTFSI)-based localized high-concentration electrolyte (LHCE) is chosen due to its stability to the oxygen cathode and the compatibility with the graphite-intercalation anode. These findings point out a promising strategy for developing practical potassium superoxide batteries with the holistic anode-electrolyte-cathode compatibility.

## Introduction

The metallic lithium (Li) is regarded as the "Holy Grail" anode in all the Li metal batteries (LMBs) due to its ultrahigh specific capacity (3860 mAh g$^{-1}$) and low redox potential (-3.04 V *vs.* the standard hydrogen electrode).[1] Nevertheless, the safety concerns related to the severe dendrite growth during Li plating/stripping render LMBs unavailable for commercialization. Among the various anode alternatives, the cost-effective graphite has won over other options because of superb cyclic stability, low voltage plateau (~0.1 V *vs.* Li$^+$/Li), and enhanced safety without dendrite growth.[2] These features make the graphite dominate the anode for the current lithium−ion batteries (LIBs).

Aprotic alkali metal−oxygen batteries have attracted intense interests recently as promising alternatives to the current LIBs due to higher theoretical energy densities and inexhaustible oxygen supply from ambient air.[3] Different from the sluggish reaction kinetics with regard to the peroxide formation/decomposition in lithium−oxygen batteries (LOBs) system, the emerging potassium−oxygen batteries (POBs) based on one-electron O$_2$/KO$_2$ redox couples have the advantages of high energy efficiencies (above 90%) without the need of electrocatalysts or redox mediator.[4-6] Especially, the formation of KO$_2$ as the sole discharge product is both kinetically and thermodynamically favourable, which enables its long-term stability.[7] Metallic potassium (K) is a desirable anode candidate for POBs due to its high theoretical specific capacity (687 mAh g$^{-1}$) and low redox potential (-2.93 V *vs.* the standard hydrogen electrode). However, the highly reactive K metal has severe side reactions with electrolytes, giving rise to low anode reversibility and potential safety hazard, just like Li metal does.[8] The problem resulting from the oxygen crossover further accelerates the accumulation of byproducts, which leads to quick anode degradation and limits the lifespan of POBs.[9] To address the abovementioned concerns, a more stable anode alternative is required. Lu's group and Zhai's group have demonstrated a long-life POB based on the dendrite-free biphenyl−K anolyte and sodium (Na)−K alloy anode, respectively.[10, 11] Wu et al. adopted the potassium−antimony (Sb) alloy anode to build the so-

a. Department of Chemistry and Biochemistry, The Ohio State University, 100 West 18th Avenue, Columbus, Ohio 43210, USA. E-mail: wu@chemistry.ohio-state.edu
b. Shenzhen Key Laboratory for Graphene-Based Materials and Engineering Laboratory for Functionalized Carbon Materials, Shenzhen Geim Graphene Center, Graduate School at Shenzhen, Tsinghua University, Shenzhen 518055, PR China. E-mail: zhaidy0404@sz.tsinghua.edu.cn

called potassium–ion oxygen batteries (PIOBs), which displays the enhanced interfacial stability and safety.[12]

Compared to Sb and other materials, graphite is still the most promising anode for K ions (K$^+$) storage due to its abundance and low flat voltage plateau (~0.24 V *vs.* K$^+$/K).[13-16] The graphite possesses the similar intercalation chemistry for K$^+$ compared with the Li ions (Li$^+$) case and delivers a theoretical specific capacity of 279 mAh g$^{-1}$, which corresponds to the formation of stage-1 K-graphite intercalation compound (GIC) of KC$_8$. Some developments in functional solid electrolyte interphase (SEI) have been made to boost K$^+$ storage capability in graphite or graphitic material.[17-20] It has been demonstrated that potassium bis(fluorosulfonyl)imide (KFSI)-based electrolyte enables the reversible intercalation of K$^+$ into graphite.[17, 18, 20-22] Therefore, it is natural to explore the possibility of using graphite anode in a PIOB. The total reaction is KC$_8$ + O$_2$ → KO$_2$ + 8 C with an e.m.f. of ~2.25 V, and the theoretical specific energy is ~360 Wh kg$^{-1}$ calculated based on both anode and cathode mass. However, our recent work has shown that KFSI reacts with KO$_2$ and thus cannot be used in a PIOB.[23] Until now, it remains a challenge to identify an electrolyte that simultaneously satisfies the anode (stable and reversible K$^+$ intercalation/de-intercalation) and the cathode (chemically stable with KO$_2$).

In this study, we first examined different salts and found that potassium bis(trifluoromethanesulfonyl)imide (KTFSI)-based electrolyte cannot allow reversible K$^+$ intercalation/de-intercalation in pristine graphite due to the K salt-lean SEI. We then developed an artificial SEI for the graphite anode and coupled with a localized high-concentration electrolyte (LHCE) to enable a reversible graphite anode and a stable KO$_2$ cathode simultaneously. The assembled PIOB possesses a high average coulombic efficiency (CE) of 98.6% with decent energy efficiencies (above 90%) over 80 stable cycles at a depth of discharge (DOD) of 25%. It is further revealed that the round-trip overpotential of the PIOB mainly comes from the graphite anode by a three-electrode electrochemical test. The artificial SEI cannot fully protect the graphite-intercalation anode from oxygen crossover, and the gradual capacity loss in graphite due to the oxygen-induced degradation is responsible for the decrease in the discharge voltage plateau of PIOB during cycles.

## Results and discussion

### Stabilizing the anode–electrolyte interface: KFSI *vs.* KTFSI

The natural flake graphite with the typical sheet-like morphology was used in this study (**Fig. S1**). Raman spectrum shows that the graphite powder has a low I$_D$/I$_G$ ratio of 0.04, demonstrating its high crystallinity in the microstructure. The suitability of different solvents was first checked before utilizing the graphite anodes for PIOBs. Organic carbonate solvents (e.g., propylene carbonate) cannot be applied in aprotic metal–oxygen batteries because they are susceptible to be attacked by the nucleophilic superoxide intermediate.[24] In comparison, the ether- and dimethyl sulfoxide (DMSO)-based electrolytes have been widely used in LOB and sodium–oxygen battery systems due to the strong resistance to the nucleophilic attack by superoxide.[25-28] Apart from being stable to the KO$_2$ cathode, the electrolyte is also required to be compatible with the graphite anode. To check the anode compatibility, the commercial KC$_8$ powder was added into 1,2-dimethoxyethane (DME) and DMSO solvents, respectively. It is observed that the bronze KC$_8$ turns to the black substance within 10 minutes, demonstrating its instability in DMSO (**Fig. S2**a). In comparison, the KC$_8$ powder still shows the golden luster in DME.

With DME as the solvent, we then examined the effect of different salts and concentrations. In a low-concentration electrolyte of 0.5 mol L$^{-1}$ (M) potassium hexafluorophosphate (KPF$_6$)/DME, solvent co-intercalation into graphite interlayer occurs with a high voltage plateau at 0.8-0.9 V (**Fig. 1**a), which lowers the voltage output of the full cell. This is consistent with a prior study by Pint and co-workers.[29] The high-concentration electrolyte (HCE) is proposed to avoid the solvent co-intercalation.[30] Due to the limited solubility in DME, the KPF$_6$ is excluded while the KFSI and KTFSI salts are good options because of their ultrahigh solubility.

The K$^+$ storage capability of graphite was then evaluated by assembling the K/graphite cells in high-concentration KFSI/DME or KTFSI/DME, respectively. Komaba has reported the highly reversible graphite anode for potassium–ion batteries using concentrated KFSI/DME (~6.91 mol kg$^{-1}$).[20] However, there is no related report on the concentrated KTFSI/DME. When the concentration is above 4 mol kg$^{-1}$ (m) for KTFSI/DME, the process of K$^+$ intercalation/de-intercalation in graphite occurs at a low voltage plateau at 0.2-0.4 V, indicating the elimination of solvent co-intercalation (**Fig. 1**b). After a quick screening process based on the reversible capacities and initial CEs of graphite electrodes, the concentration is chosen at 5m for KTFSI/DME (See the detailed information in **Fig. S2**b), which is used as the control sample. It is further revealed that the graphite in 6.91m KFSI/DME shows a reversible capacity of 262.0 mAh g$^{-1}$ after the 2$^{nd}$ cycle and 252.5 mAh g$^{-1}$ after the 100$^{th}$ cycle with a capacity retention of 96.4%, indicating its superb cyclic stability (**Fig. 1**c-d). The capacity is very close to the theoretical value of the Stage-1 K-GIC of KC$_8$ (279 mAh g$^{-1}$).[2] In comparison, the reversible capacity of graphite in 5m KTFSI/DME is 101.3 mAh g$^{-1}$ after the 2$^{nd}$ cycle, and only the capacity of 21.6 mAh g$^{-1}$ is achieved after 100 cycles. X-ray diffraction (XRD) measurements were conducted to identify the formed GICs. It is found that the potassiated graphite with the typical bronze colour is composed of the dominating KC$_8$ and the slight KC$_{24}$ in 6.91m KFSI/DME (**Fig. 1**e). In comparison, the bronze substance only distributes at the partial region of graphite in 5m KTFSI/DME, and the Stage-2 GICs of KC$_{24}$ are the main products. The insufficient K$^+$ intercalation into graphite interlayer results in a reduced capacity in 5m KTFSI/DME.

# ARTICLE
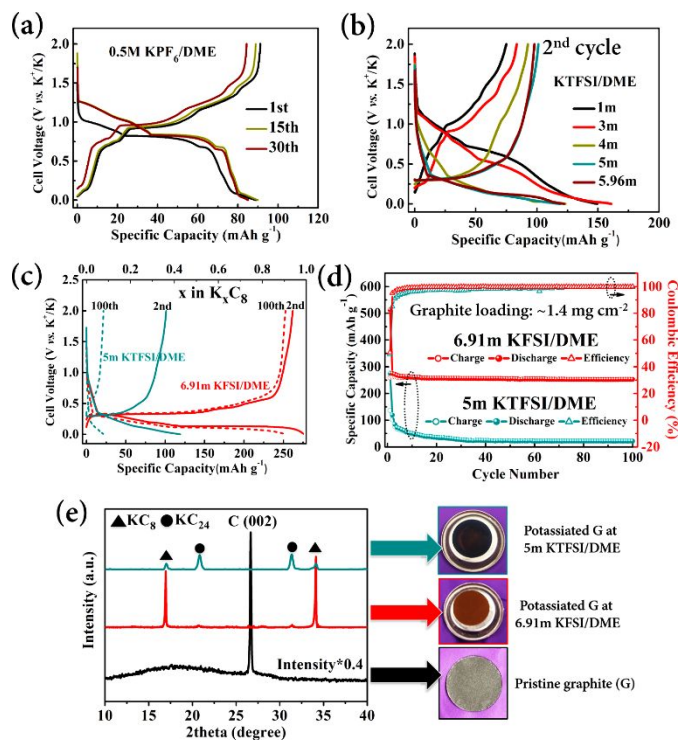


**Fig. 1** Electrochemical behaviour of K/graphite cells and potassiated graphite identification in different electrolytes. Typical voltage profiles of K/graphite cells in (a) 0.5M $KPF_6$/DME and (b) KTFSI/DME with different concentrations. (c) The specific 2nd and 100th voltage profiles, and (d) long-term cyclic stability of K/graphite cells in 6.91m KFSI/DME (red) and 5m KTFSI/DME (cyan). The current density for the cells is 50 mA $g^{-1}$, which corresponds to ~0.18 C rate (1 C=279 mA $g^{-1}$). (e) XRD patterns and optical images of pristine graphite and potassiated graphite (after 2nd discharge).

The different SEI components formed on the graphite surface and their effect on the electrochemical performance were then investigated. The graphite delivers a reversible capacity of 259.4 mAh $g^{-1}$ (initial CE = 50.6%) in 6.91m KFSI/DME, while it only shows a low reversible capacity of 136.8 mAh $g^{-1}$ (initial CE = 49.8%) in 5m KTFSI/DME (**Fig. 2**a). The first cyclic voltammetry (CV) scans indicate that there are additional reduction peaks for KFSI/DME (at 0.4-1.2 V) and KTFSI/DME (at 0.4-1.0 V), which corresponds to the SEI formation and accounts for the first irreversible capacity (**Fig. 2**b). X-

ray photoelectron spectroscopy (XPS) was conducted to analyse the SEI components. It is revealed that the contents of K, O, F, and S elements increase dramatically compared to those in pristine graphite, which is due to the formed SEI in 6.91m KFSI/DME (**Fig. 2**c). As evidenced in the F 1s spectrum, the dominating K-F species (682.8 eV) and minor S-F species (687.7 eV) are identified, implying that the S-F groups in FSI$^-$ anions tend to have bond cleavage to form KF during SEI formation (**Fig. 2**d). It is shown in the S 2p spectrum that there are two sulfur-related species, which are assigned to the potassium sulfate ($KSO_x$) species and the $-SO_2-$ fragment (**Fig. 2**e). The formation of these sulfur-containing species may result from the cleavage of the N-S bond.[31] In addition to the adventitious C-C peak, the C 1s spectrum confirms the existence of C=O species, which originates from DME decomposition (**Fig. S3**a). Meanwhile, the C=O, S=O, and oxide species are observed from the O 1s signal (**Fig. S3**b), which agrees well with the previous discussion. Therefore, the formed SEI components in 6.91m KFSI/DME mainly derive from FSI$^-$ anions decomposition and such layer mainly contains potassium sulfate/sulfur oxide species, KF, and carbonyl species. Energy-dispersive X-ray spectroscopy (EDS) shows that K, O, S, and F elements in the SEI distribute uniformly across the graphite surface (**Fig. S4**).

The formed SEI in 5m KTFSI/DME exhibits similar components except for the slight differences in specific species. The dominant K-F species (682.9 eV) and the minor C-F species (688.7 eV) are identified in the F 1s spectrum, indicating that the $CF_3$ groups in TFSI$^-$ can occur C-F bond cleavage to form KF. Despite that, the relative contents of F, S, and K elements on the graphite surface in KTFSI/DME are much lower than those in KFSI/DME. The difference in component contents in the SEIs is related to the decomposition pathways of anions. The decomposition of FSI$^-$ anions occurs through the cleavage of both N-S bond and S-F bond, whereas TFSI$^-$ anions decompose through the cleavage of N-S and C-F bonds. Based on the observation that the SEI derived from TFSI$^-$ anions contains less K content than that from FSI$^-$ anions (**Fig. 2**c), we propose that the SEI formed in KTFSI-based electrolyte is not a good ionic conductor for K$^+$ and cannot prevent the further parasitic reactions, which is also evidenced by the increased impedance upon cycles (**Fig. S5**). A similar conclusion is drawn in our prior study on metallic K anode based on KTFSI/DME electrolyte.[32] In comparison, the resistance values do not change much in 6.91m KFSI/DME, indicating more stable interfaces of graphite/electrolyte and K/electrolyte.

# ARTICLE
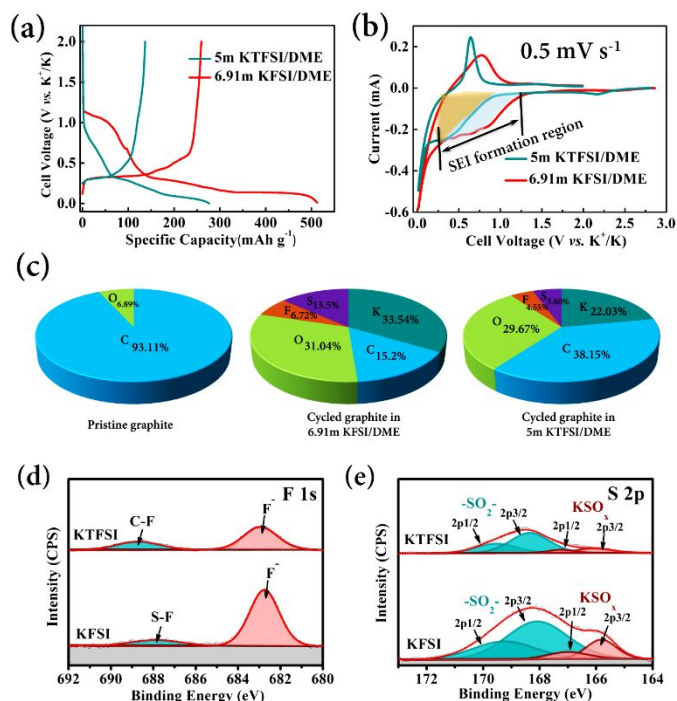


Fig. 2 Characterization of SEI components in high-concentration KFSI- and KTFSI-based electrolytes. (a) First discharge/charge voltage profiles and (b) initial CV curves of graphite electrodes from K/graphite cells in 6.91m KFSI/DME (red) and 5m KTFSI/DME (cyan). The CV scan rate is 0.5 mV s$^{-1}$. (c) The atomic contents (at.%) of pristine graphite and cycled graphite. XPS spectra of the (d) F 1s and (e) S 2p regions on the cycled graphite surface (after 1$^{st}$ charge) in 5m KTFSI/DME (up) and 6.91m KFSI/DME (down). The thick red lines represent the fitted results.

## Artificial SEI strategy to simultaneously stabilize graphite anode and KO$_2$ cathode

Although the graphite shows excellent reversibility, the KFSI-based electrolyte cannot be used in the PIOBs due to the instability of FSI$^-$ anion in the presence of superoxide.[23] It requires us to utilize other salts (e.g., KTFSI) to ensure electrolyte stability. Nevertheless, graphite anode delivers poor reversibility in 5m KTFSI/DME due to the formed SEI lean in K salts (KF, KSO$_x$). It seems challenging to adopt one salt to meet all the requirements. For solving the dilemma, it is proposed to establish an artificial SEI to enhance the reversibility of graphite anode while using another stable electrolyte in the PIOBs (See **Scheme 1**). In specific, the first step is to utilize the KFSI-based electrolyte to pre-form an artificial SEI on the graphite in a K/graphite cell followed by the potassiation. The potassiated graphite with the pre-formed SEI is then transferred into a PIOB using the KTFSI-based electrolyte. In this way, the advantage of KFSI for forming a stable SEI
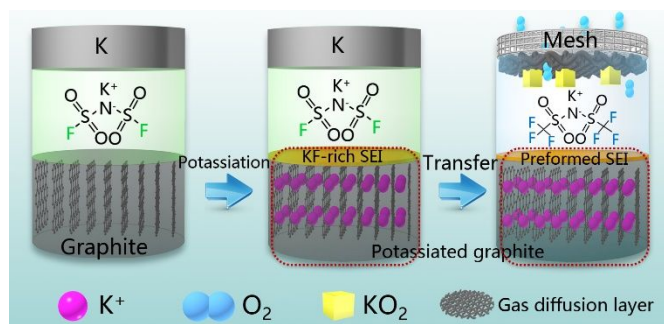


**Scheme 1.** Formation of the artificial SEI on the graphite surface to enhance its reversibility while retaining electrolyte stability in PIOBs.

on the graphite surface can be combined with the advantage of KTFSI for its stability in superoxide batteries.

The compatibility of artificial SEI with KTFSI-based electrolytes was first examined in a K/graphite cell (**Fig. 3**a). To further solve the poor electrolyte wettability and reduce the cost, a low-polarity co-solvent of highly fluorinated ether (HFE, 1,1,2,2-tetrafluoroethyl-2,2,2-trifluoroethyl ether) is applied to dilute the 5m KTFSI/DME to form an LHCE. It is observed that the cycled graphite anode with the pre-formed SEI exhibits a low voltage plateau in an HCE of KTFSI/DME and an LHCE of KTFSI/DME-HFE, implying that only K$^+$ are intercalated into graphite interlayer (**Fig. 3**b). In comparison, the typical solvent co-intercalation still occurs in 1m KTFSI/DME even when the artificial SEI is pre-formed on the graphite (**Fig. S6**). **Fig. S7** compares the Raman spectra of KTFSI-based electrolytes to understand their solvation structures. The DME solvent exhibits typical peaks located at 821 and 848 cm$^{-1}$ for CH$_2$ rocking and C-O stretching vibration, respectively. Two additional peaks occur at 835 and 859 cm$^{-1}$ after dissolving KTFSI in DME and keep growing with the increase in salt concentration when more DME molecules participate in K$^+$ solvation. The LHCE sample exhibits the similar Raman peaks of the HCE expect for the signals of co-solvent HFE at 650-670 and 867 cm$^{-1}$. That indicates that the introduction of HFE does change the local coordination structure of K$^+$. The Raman peak at 740-743 cm$^{-1}$ can be assigned to the solvated TFSI anions. In the dilute KTFSI/DME, most TFSI exists as free anions due to the high dissociation of KTFSI salt and strong coordinating ability of DME with K$^+$. While in the concentrated electrolytes, the TFSI peak shifts to a higher wavenumber and behaves more like the KTFSI solid. It is thought that there is direct interaction between TFSI$^-$ and K$^+$ in an HCE or LHCE. This clearly shows the different solvation structures around cations between an LCE and an HCE or LHCE.

The long-term stability of graphite in the KTFSI-based LHCE is also evaluated. The pristine graphite delivers poor cyclic stability in 2.32m KTFSI/DME-HFE and the reversible capacity quickly decreases to 60.1 mAh g$^{-1}$ after 20 cycles (**Fig. S8**). In comparison, the pre-cycled graphite anode with the artificial SEI shows excellent cyclic stability

with a reversible capacity of 249.6 mAh g$^{-1}$ even after 600 cycles (**Fig. 3**c). *Ex-situ* XRD measurements were further conducted to monitor the structural evolution of pre-cycled graphite during K$^+$ intercalation/de-intercalation (**Fig. S9**). It is observed that there are multiple stage phases of K-GICs and the phase transition of graphite upon K$^+$ insertion follows the pathway: graphite→ high-order stage GICs (＞stage 3)→ stage 3 GICs (KC$_{36}$)→ stage 2 GICs (KC$_{24}$)→ stage 1 GICs (KC$_8$). In addition, the phase transition of K-GICs takes place in an opposite sequence and is highly reversible during K$^+$ extraction, which is evidenced by the stepwise disappearance of low-stage phases and the final appearance of the characteristic (002) peak of graphite. Based on our research results, it is concluded that both the solvation structures of K$^+$ and the SEI are crucial factors to affect the intercalation chemistry when forming the binary GICs. And the pre-formed SEI in an HCE of KFSI/DME can stabilize the graphite anode and sustain the reversible K$^+$ intercalation/de-intercalation in an LHCE of KTFSI/DME-HFE.

To evaluate the electrolyte stability in the PIOB, the commercial KO$_2$ powder was added into the LHCE to mimic the possible chemical reaction in the POB environment, and the products after aging were characterized by nuclear magnetic resonance (NMR) spectroscopy (**Fig. S10**). $^{19}$F NMR spectra indicate that there are no chemical shifts in the TFSI$^-$ (σ = -79 ppm) and HFE (σ$_a$ = -75 ppm, σ$_b$ = -93 ppm, σ$_c$ = -137 ppm), thus implying its superb chemical stability. Therefore, the proposed LHCE of KTFSI/DME-HFE is demonstrated to be stable with KO$_2$ cathode and is compatible with anode if an artificial SEI is pre-formed on the graphite surface.
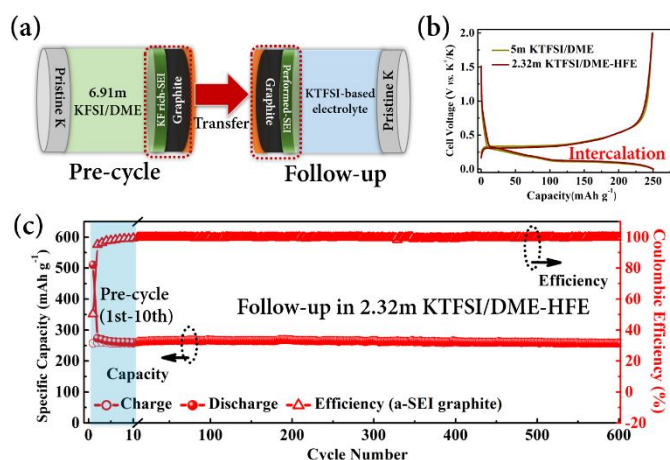


**Fig. 3** The effect of artificial SEI on improving graphite reversibility in KTFSI-based electrolyte. (a) Schematic illustration of pre-forming an artificial SEI on the graphite surface. (b) Voltage profiles of cycled graphite electrodes with artificial SEI from K/graphite cells in 5m KTFSI/DME (dark yellow) and 2.32m KTFSI/DME-HFE (1:2.27:1.13 by mol) (wine). (c) Cycling performance and efficiencies of K/graphite cells with artificial SEI pre-formed on the graphite (pre-cycling in 6.91m KFSI/DME for 10 cycles as shown in the shadow region) in

2.32m KTFSI/DME-HFE. The applied current is 50 mA g$^{-1}$ (0.18 C) and calculated based on the mass of graphite.

### Potassium−ion oxygen batteries under controlled DOD

To prove the strategy in the PIOB, the potassiated graphite anode was coupled with a carbon paper cathode in the LHCE. XRD patterns show that crystalline KO$_2$ is formed on the cathode after discharge, which disappears after the following charge (**Fig. S11**). SEM images of the discharged cathode indicate that the numerous cubic-shaped KO$_2$ particles are found on the surface of carbon fibre substrates (**Fig. S12**a-e). When the cell is charged to 3.0 V, the electrochemical formed KO$_2$ cubes are largely removed (**Fig. S12**f-j). Only a film-like residue is left on the surface, which is ascribed to the side products and "dead" KO$_2$ according to our prior study.[6, 7] The above results indicate the reversible redox of O$_2$/KO$_2$ at the cathode.

For cyclic stability evaluation, the reversible capacity of potassiated graphite (1.4 mg cm$^{-2}$) is around 0.4 mAh. Since the cycling capacity is curtailed at 0.1 mAh, the DOD is 25% for the PIOB, which displays a pronounced discharge platform at 2.2 V with the initial CE of 81.7% (**Fig. 4**a). Despite that the cell exhibits a gradual decrease in the discharge platforms (ca. 2.15 V at 40$^{th}$ cycle, 2.1 V at 60$^{th}$ cycle and 2.0 V at 78$^{th}$ cycle), a small round-trip overpotential of 0.19~0.24 V is achieved during cycles, which implies high energy efficiencies (above 90%). With the artificial SEI pre-formed on the potassiated graphite anode, the PIOB shows over 80 stable cycles with a high average CE of 98.6% (**Fig. 4**b).

The discharge process of the PIOB corresponds to the extraction of K$^+$ from graphite, and the K$^+$ would intercalate into the graphite interlayer during the charging procedure. Herein, the potassiation/depotassiation processes are divided into different segments based on different DODs (**Fig. 4**c). At a DOD of 25%, the potential change in the potassiated graphite anode should follow the trend shown in the red segment (0.75~1). In this segment, the depotassiation potential locates at around 0.3 V (*vs.* K$^+$/K). This can explain the lower first discharge platform (around 2.2 V) in the PIOB in comparison to the theoretical value (2.48 V, K + O$_2$ → KO$_2$).

To further monitor the potential change of anode and cathode separately, a three-electrode setup is used with a metallic K wire as the reference electrode (**Fig. 4**d). At a deep DOD of 87.5%, the KO$_2$ formation and decomposition only delivers a round-trip overpotential of 58 mV at the cathode (estimated by measuring the middle potential point in the discharge/charge processes), illustrating the superb reaction kinetics of O$_2$/KO$_2$ redox. In comparison, the round-trip overpotentials between the potassiation/depotassiation are around 150~200 mV at the anode, which implies that the round-trip overpotential of PIOB mainly comes from the graphite anode. Note that the round-trip overpotentials in graphite are slightly lower compared to those in a two-electrode K/graphite cell (**Fig. 4**c), which is ascribed to the elimination of polarization from the K reference electrode in a three-electrode setup.

# ARTICLE
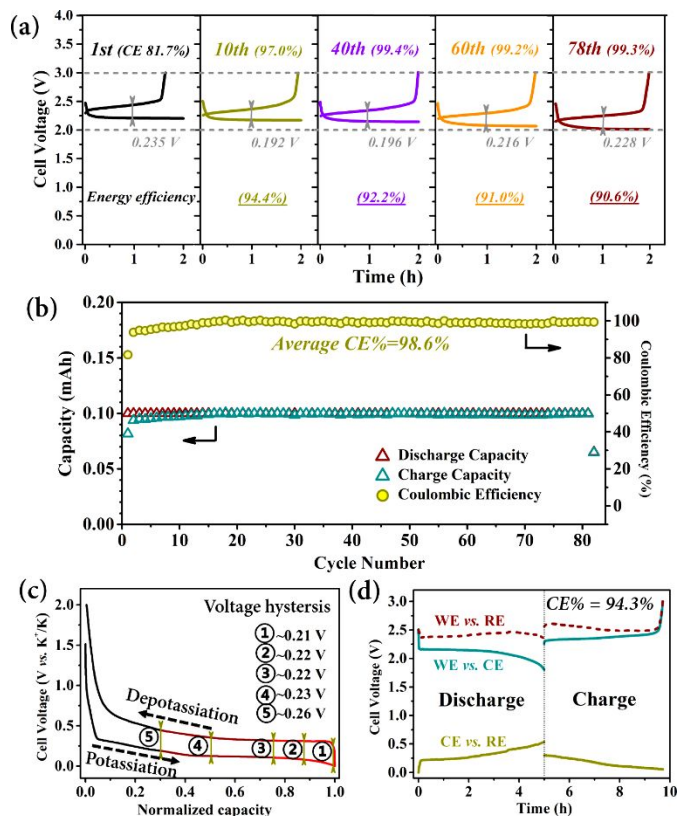


**Fig. 4** Electrochemical behaviour of PIOBs under controlled DOD. (a) Specific voltage profiles and (b) Cyclic stability and CEs of the PIOB based on potassiated graphite anode in 2.32m KTFSI/DME-HFE (1:2.27:1.13 by mol). The current is 0.05 mA with a curtailed capacity of 0.1 mAh. (c) Voltage profile of the K/graphite cell in 2.32m KTFSI/DME-HFE. The graphite with artificial SEI was the anode. (d) First discharge/charge profiles of the PIOB with a three-electrode setup. (Working electrode: carbon paper; Counter electrode: potassiated graphite with artificial SEI; Reference electrode: potassium wire sealed in a PEEK sleeve.) The current is 0.07 mA with a curtailed discharge capacity of 0.35 mAh.

Post-mortem XPS measurements were conducted to reveal the change in the SEI component on the graphite anode during cycling. It is revealed that the artificial SEI still mainly contains $KSO_x$, KF, sulfur oxide species, and carbonyl species after cycles (**Fig. S13**). Nevertheless, the S-F species cannot be identified while the $CF_x$ species (688.6 eV) are observed in the F 1s spectrum, indicating the decomposition of $TFSI^-$ (**Fig. 5**). Compared to that in pristine artificial SEI (**Fig. 2**c), the O element content increases obviously, which indicates that the artificial SEI cannot adequately protect the potassiated graphite from parasitic reactions with electrolyte and oxygen crossover during cycling. XRD results confirm that the relative intensity ratio of Stage-2 GICs ($KC_{24}$) to Stage-1 GICs ($KC_8$) in the
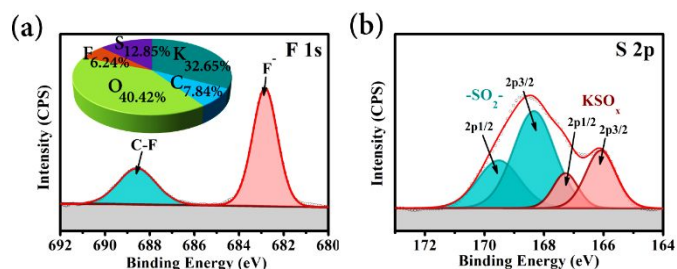


**Fig. 5** Post-mortem XPS analyses on the artificial SEI. XPS spectra of the (a) F 1s region and (b) S 2p region on the cycled graphite surface in the PIOB. The inset in **5**a is the atomic contents (at.%) of SEI components on the cycled graphite.

anode increases after cycles, which implies the anode degradation induced by oxygen crossover (**Fig. S14**). As a result, the graphite-intercalation anode exhibits a continuous K loss and capacity decay during cycling. Therefore, the depotassiation potential increases, which accounts for the gradual decrease in the discharge voltage plateaus of PIOB (**Fig. 4**a). Based on the above observations, it is concluded that the artificial SEI derived from KFSI decomposition stabilizes the graphite/electrolyte interface, but such SEI still shows a limited protection effect on graphite-intercalation anode from oxygen crossover during long-term cycles. An oxygen-blocking separator is expected to further boost the PIOB performance, which is subject to further investigation.

As a final note, there is a potential safety hazard when handling the reactive potassiated graphite. It reacts with water and produces flammable hydrogen gas. Our recent reports reveal that $KO_2$ is highly stable in dry ambient air.[6, 33] This provides the possibility to assemble the graphite/$KO_2$ cell in a battery dry room that represents the fully discharged state. This also avoids handling the reactive potassiated graphite anode with much enhanced safety and is more compatible with the current dry-room manufacturing technology.

## Conclusions

In summary, this study presents an effective approach for building an artificial SEI to enable reversible graphite anodes while circumventing electrolyte decomposition in the PIOBs. Due to the cleavage of S-F and N-S bonds in $FSI^-$ anions, a stable K salt-rich SEI is formed on the graphite surface, which helps to realize reversible $K^+$ intercalation/de-intercalation processes. An LHCE recipe (KTFSI: DME: HFE, 1:2.27:1.13 by molar ratio) is applied in the PIOB demonstration because such the electrolyte possesses a unique solvation structure, which enables it to be compatible with graphite anode while maintaining the $KO_2$ cathode stability. The PIOB shows high energy efficiencies (above 90%) and a lifespan of over 80 stable cycles at a DOD of 25%. The round-trip overpotential of PIOB mainly comes from the graphite anode. It is further revealed that the artificial SEI cannot adequately protect the graphite-intercalation

anode from oxygen crossover, and the anode degradation is responsible for the battery deterioration. Our work paves the way to develop promising graphite anodes for practical $KO_2$-based superoxide batteries, where a high DOD and K metal-free anode are indispensable.

## Conflicts of interest

The authors declare no competing financial interests.

## Acknowledgements

## Notes and references

1. X.-B. Cheng, R. Zhang, C.-Z. Zhao and Q. Zhang, *Chem. Rev.*, 2017, **117**, 10403-10473.
2. Y. Li, Y. Lu, P. Adelhelm, M.-M. Titirici and Y.-S. Hu, *Chem. Soc. Rev.*, 2019, **48**, 4655-4687.
3. W. Zhang, Y. Huang, Y. Liu, L. Wang, S. Chou and H. Liu, *Adv. Energy Mater.*, 2019, **9**, 1900464.
4. X. Ren and Y. Wu, *J. Am. Chem. Soc.*, 2013, **135**, 2923-2926.
5. N. Xiao, X. Ren, W. D. McCulloch, G. Gourdin and Y. Wu, *Acc. Chem. Res.*, 2018, **51**, 2335-2343.
6. L. Qin, N. Xiao, S. Zhang, X. Chen and Y. Wu, *Angew. Chem. Int. Ed.*, 2020, **59**, 10498-10501.
7. N. Xiao, R. T. Rooney, A. A. Gewirth and Y. Wu, *Angew. Chem. Int. Ed.*, 2018, **57**, 1227-1231.
8. L. Qin, Y. Lei, H. Wang, J. Dong, Y. Wu, D. Zhai, F. Kang, Y. Tao and Q.-H. Yang, *Adv. Energy Mater.*, 2019, **9**, 1901427.
9. X. Ren, K. C. Lau, M. Yu, X. Bi, E. Kreidler, L. A. Curtiss and Y. Wu, *ACS Appl. Mater. Interfaces*, 2014, **6**, 19299-19307.
10. G. Cong, W. Wang, N.-C. Lai, Z. Liang and Y.-C. Lu, *Nat. Mater.*, 2019, **18**, 390-396.
11. W. Yu, K. C. Lau, Y. Lei, R. Liu, L. Qin, W. Yang, B. Li, L. A. Curtiss, D. Zhai and F. Kang, *ACS Appl. Mater. Interfaces*, 2017, **9**, 31871-31878.
12. W. D. McCulloch, X. Ren, M. Yu, Z. Huang and Y. Wu, *ACS Appl. Mater. Interfaces*, 2015, **7**, 26158-26166.
13. Z. Jian, W. Luo and X. Ji, *J. Am. Chem. Soc.*, 2015, **137**, 11566-11569.
14. Y. Chen, L. Qin, Y. Lei, X. Li, J. Dong, D. Zhai, B. Li and F. Kang, *ACS Appl. Mater. Interfaces*, 2019, **11**, 45578-45585.
15. Y. Lei, L. Qin, R. Liu, K. C. Lau, Y. Wu, D. Zhai, B. Li and F. Kang, *ACS Appl. Energy Mater.*, 2018, **1**, 1828-1833.
16. Y. Lei, D. Han, J. Dong, L. Qin, X. Li, D. Zhai, B. Li, Y. Wu and F. Kang, *Energy Storage Mater.*, 2020, **24**, 319-328.
17. L. Fan, R. Ma, Q. Zhang, X. Jia and B. Lu, *Angew. Chem. Int. Ed.,* 2019, **58**, 2-8.
18. L. Qin, N. Xiao, J. Zheng, Y. Lei, D. Zhai and Y. Wu, *Adv. Energy Mater.*, 2019, **9**, 1902618.
19. J. Hui, N. B. Schorr, S. Pakhira, Z. Qu, J. L. Mendoza-Cortes and J. Rodriguez-Lopez, *J. Am. Chem. Soc.*, 2018, **140**, 13599-13603.
20. T. Hosaka, K. Kubota, H. Kojima and S. Komaba, *Chem. Commun.*, 2018, **54**, 8387-8390.

21. S. Liu, J. Mao, Q. Zhang, Z. Wang, W. K. Pang, L. Zhang, A. Du, V. Sencadas, W. Zhang and Z. Guo, *Angew. Chem. Int. Ed.*, 2020, **59**, 3638-3644.
22. J. Zhang, Z. Cao, L. Zhou, G. Liu, G.-T. Park, L. Cavallo, L. Wang, H. N. Alshareef, Y.-K. Sun and J. Ming, *ACS Energy Lett.*, 2020, **5**, 2651-2661.
23. N. Xiao, G. Gourdin and Y. Wu, *Angew. Chem. Int. Ed.*, 2018, **57**, 10864-10867.
24. S. A. Freunberger, Y. Chen, Z. Peng, J. M. Griffin, L. J. Hardwick, F. Barde, P. Novak and P. G. Bruce, *J. Am. Chem. Soc.*, 2011, **133**, 8040-8047.
25. L. Qin, D. Zhai, W. Lv, W. Wei, W. Yu, Y. Lei, W. Yang, J. Huang, S. Yao, J. Cui, F. Kang, J.-K. Kim and Q.-H. Yang, *Energy Storage Mater.*, 2017, **9**, 134-139.
26. M. He, K. C. Lau, X. Ren, N. Xiao, W. D. McCulloch, L. A. Curtiss and Y. Wu, *Angew. Chem. Int. Ed.,* 2016, **55**, 15310-15314.
27. M. M. Ottakam Thotiyl, S. A. Freunberger, Z. Peng and P. G. Bruce, *J. Am. Chem. Soc.*, 2013, **135**, 494-500.
28. J. Kim, H. Park, B. Lee, W. M. Seong, H.-D. Lim, Y. Bae, H. Kim, W. K. Kim, K. H. Ryu and K. Kang, *Nat. Commun.*, 2016, **7**, 10670.
29. A. P. Cohn, N. Muralidharan, R. Carter, K. Share, L. Oakes and C. L. Pint, *J. Mater. Chem. A*, 2016, **4**, 14954-14959.
30. Y. Yamada, J. Wang, S. Ko, E. Watanabe and A. Yamada, *Nat. Energy*, 2019, **4**, 269-280.
31. N. Xiao, W. D. McCulloch and Y. Wu, *J. Am. Chem. Soc.*, 2017, **139**, 9475-9478.
32. X. Ren, M. He, N. Xiao, W. D. McCulloch and Y. Wu, *Adv. Energy Mater.*, 2017, **7**, 1601080.
33. L. Qin, L. Schkeryantz, J. Zheng, N. Xiao and Y. Wu, *J. Am. Chem. Soc.*, 2020, **142**, 11629-11640.